Research Papers

GREENSUSMATER

Greensusmater
Vol. 3, No. 2, 2026
https://doi.org/10.62755/gsm.2026.08

Check for updates

# Equal Surface Oxygen, Different Adsorbent: Ammonium Persulfate Demineralises NaOH-Activated Plastic Pyrolytic Char While Hydrogen Peroxide Does Not

Nabila Putri Insani[1,†], Michelle Simanjuntak[1,†], Asri Saffanah Pratiwi[2], Sephia Amanda Muhtar[3], Adri Huda[4], Irwan Kurnia[5], Joko Waluyo[6], Tarmizi Taher[1,2,*]

[1] *Department of Environmental Engineering, Faculty of Infrastructure and Regional Technology, Institut Teknologi Sumatera, Terusan Ryacudu, Way Hui, Jati Agung, Lampung Selatan 35365, Indonesia*
[2] *Center for Green and Sustainable Materials, Institut Teknologi Sumatera, Terusan Ryacudu, Way Hui, Jati Agung, Lampung Selatan 35365, Indonesia*
[3] *Department of Environmental Engineering, Institut Teknologi Bandung, Bandung, Indonesia*
[4] *Department of Environmental Engineering, Faculty of Engineering, Universitas Sumatera Utara, Medan, Indonesia*
[5] *Department of Chemistry, Faculty of Mathematics and Natural Sciences, Universitas Padjadjaran, Sumedang, Indonesia*
[6] *Department of Chemical Engineering, Universitas Sebelas Maret, Surakarta, Indonesia*
[†] *These authors contributed equally to this work.*

**Corresponding author**: tarmizi.taher@itera.ac.id

ARTICLE HISTORY: Received: July 31, 2026 | Revised: September 10, 2026 | Accepted: September 16, 2026

## ABSTRACT

Oxidative post-treatment of alkali-activated char is normally assessed by how much oxygen it adds to the carbon surface, so the inorganic fraction, which in a high-ash char makes up most of the solid, is rarely tracked separately. We treated NaOH-activated plastic pyrolytic char (PPC) with either $H_2O_2$ or ammonium persulfate (AP) and characterised the carbon and the mineral matrix independently. By the two measures normally used to describe an oxidised surface, the two oxidants are indistinguishable: the atomic O/C ratio reaches 0.457 and 0.455, and the zeta potential reaches $-35.0 \pm 3.0$ and $-36.7 \pm 3.4$ mV ($n$ = 7), equivalent within 5 mV by two one-sided tests. The mineral matrix separates them. Thermogravimetry in air places the ash content of the activated char at 60.7 wt%, which falls to 52.1 wt% after $H_2O_2$ treatment and to 16.8 wt% after AP treatment. X-ray diffraction shows that the $H_2O_2$-treated char retains its crystalline assemblage, whereas AP treatment removes the calcite that survives $H_2O_2$ and reduces the assemblage to traces of quartz and rutile over a turbostratic carbon hump at $d_{002}$ = 3.58 $\pm$ 0.07 Å. Scaled by ash content, the AP route depletes every major mineral element by 67–88%, compared with 0–56% for $H_2O_2$. The apparent methylene blue capacity at 120 min rises from 44.7 to 57.6 mg $g^{-1}$ after $H_2O_2$ treatment but only from 113.7 to 120.2 mg $g^{-1}$ on an ash-free basis, and the two oxidised chars respond differently to solution pH. The AP route is carried out in 2 M $H_2SO_4$, so its effects are attributed to the route as practised rather than to persulfate alone. Surface oxygen content and surface charge therefore do not predict what an oxidant has done to a high-ash char, and reporting either alone leaves the larger structural change unrecorded.

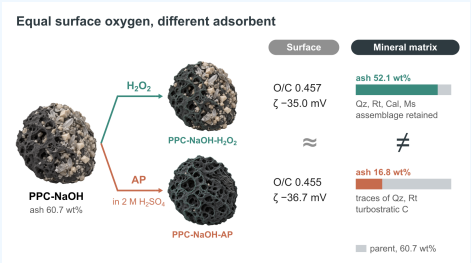


**Keywords**: *Plastic Pyrolytic Char; NaOH Activation; Ammonium Persulfate; Demineralisation; Surface Oxidation; Methylene Blue Adsorption*

## 1. INTRODUCTION

Pyrolysis of mixed-plastic waste yields a solid residue, plastic pyrolytic char (PPC), whose output scales with the process itself and for which few uses exist [1,2,3,4]. Converting it into an adsorbent is attractive because the alternative is landfill, but PPC is a poor starting material: it carries a large inorganic load inherited from fillers and additives in the feed plastics [5,3], and its as-received surface area is negligible [6,7]. That load survives processing: an activated carbon prepared from municipal plastic waste retains 38.3% ash, which its authors assign to plastic fillers and pigments together with residue from the activating agent [8]. Nor is PPC interchangeable with biomass-derived biochar, whose upgrading routes assume a carbon-rich precursor [9,10].

Alkali activation addresses the surface area. Impregnation with KOH or NaOH followed by heating under inert gas develops porosity through a combination of carbon gasification and alkali intercalation into the carbon lattice [11,12], and NaOH activation of a carbon-rich precursor by this route reaches 1508.6 $m^2/g$ [13]. Applied to plastic pyrolysis char, it yields usable adsorbents for dyes and metal ions [14,15,16,17]. The step does not, however, remove the inorganic fraction. In the material studied here, the acid-washed NaOH-activated char retains a mineral assemblage of quartz, rutile, calcite and mica.

A second, oxidative treatment is therefore common and is normally justified by the oxygen-bearing functional groups it grafts onto the carbon: $H_2O_2$ and persulfate salts both raise surface oxygen content [18,19,20] and both improve uptake of cationic dyes [21]. These treatments are usually accompanied by characterisation of the carbon surface and little else: the O/C ratio, the functional-group inventory, and the point of zero charge or zeta potential [22,23,24]. Persulfate-modified activated carbon has been characterised by nitrogen sorption and infrared spectroscopy alone. Its surface area fell from

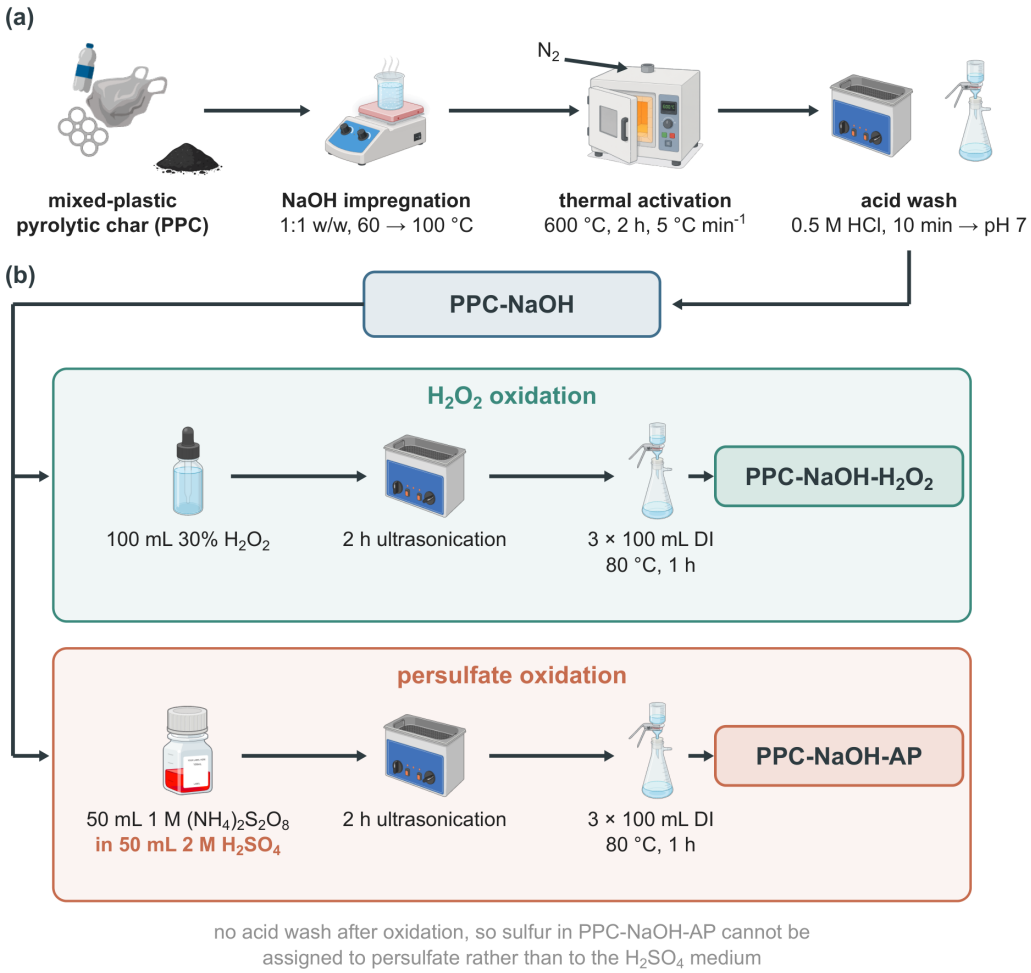


**Figure 1.** Preparation of the NaOH-activated PPC series. (a) Activation: mixed-plastic pyrolytic char is impregnated with NaOH (1:1 w/w), heated to 600 °C under $N_2$, and washed with 0.5 M HCl to give PPC-NaOH. (b) The two oxidative post-treatments applied to PPC-NaOH. Ammonium persulfate is delivered in 2 M $H_2SO_4$, and neither product is acid-washed after oxidation, so sulfur retained by PPC-NaOH-AP cannot be assigned to persulfate rather than to the acid medium.

1099 to 974 $m^2/g$ during treatment, and the decrease was attributed to persulfate entering the pores with no elemental measurement to locate it [25]. $H_2O_2$- and $HNO_3$-treated biochars have been characterised by a battery of techniques that includes thermogravimetry, but the thermogravimetry was run under nitrogen to assess thermal stability rather than under air to determine ash [26]. The same pattern holds where persulfate raises vapour uptake [27] and where $H_2O_2$ raises anion uptake [28].

Where the inorganic fraction has been measured, it has changed the measured uptake. Removing ash from a commercial activated carbon with HF and HCl raises its uptake of aromatic solutes, because ash blocks micropores that deashing reopens [29]; washing an $H_2SO_4$-activated sludge carbon with HCl raises methylene blue uptake from 82 to 98.9 mg/g, an increase its authors assign to the removal of ash rather than to a change in surface chemistry [30]. In fields that treat mineral matter as a variable, the practice is established: char oxidation reactivity is reported against demineralisation rates measured element by element [31], and $CO_2$ uptake by coals spanning 6.1 to 39.4% ash is reported on dry-ash-free and mineral-matter-free bases [32].

Table 1 locates the gap between these two bodies of work. Of twelve studies of oxidised or alkali-activated carbons, four quantify the inorganic fraction separately from the carbon, and two of those four come from char-combustion and coal research rather than from water treatment. The remainder identify mineral phases without weighing them. In one NaOH-activated carbon, silica is identified by infrared spectroscopy, diffraction and electron microscopy and then discussed as a control on porosity and uptake without being quantified. In a tyre char, diffraction with an internal standard is used to fit the carbon (002) peak, while the zinc and potassium reflections beside it are left unindexed. In a third study, ash is determined on the char but not on the activated carbon made from it, even though the activation step includes an acid wash. In a solid whose ash approaches or exceeds half its mass, an oxidant that dissolves the mineral matrix changes the material far more than one that grafts oxygen onto its carbon, and a capacity reported per gram of adsorbent cannot separate the two.

Herein, we treat NaOH-activated PPC with $H_2O_2$ or with ammonium persulfate and characterise the carbon surface and the mineral matrix independently. Methylene blue, both a persistent water contaminant [33,34] and a standard cationic probe of adsorbent surfaces [35,36,37], is then used to com-

 

pare the two products in application. The two oxidants are matched on the conventional surface descriptors but separated by the inorganic assemblage, which identifies demineralisation, not oxygen grafting, as the property that distinguishes them.

## 2. MATERIALS AND METHODS

### 2.1 Materials

Pyrolytic char derived from mixed-plastic waste pyrolysis (PPC) was used as the carbon precursor; the char and its source facility have been described previously [14]. The characterisation and adsorption data for the untreated PPC (X-ray diffraction, thermogravimetry, XRF, EDS, FTIR, zeta potential and methylene blue uptake) were first reported in [41] and are reused here as the reference for the NaOH-activated series. Sodium hydroxide (NaOH, $\geq$ 97%, Merck), hydrochloric acid (HCl, 37%, Merck), hydrogen peroxide ($H_2O_2$, 30%, Merck), ammonium persulfate ($(NH_4)_2S_2O_8$, $\geq$ 98%, Merck), sulfuric acid ($H_2SO_4$, 96–98%, Merck), Triton X-100 (Sigma-Aldrich), and methylene blue (MB, CI 52015, Merck) were of analytical grade and used without further purification. Deionised water (resistivity $\geq$ 18.2 $M\Omega$·cm) was used throughout.

### 2.2 NaOH Activation

PPC (2 g) was mixed with NaOH (2 g, mass ratio 1:1) in 15 mL of deionised water with 1.5 µL of Triton X-100 as a wetting agent. The slurry was stirred at 400 rpm for 15 min, then at 300 rpm and 60 °C for a further 30 min, then held at 100 °C until the water had evaporated (approximately 3 h). The solid was dried at 105 °C for 5 h and ground with a mortar and pestle.

The impregnated char was activated in a tube furnace under nitrogen (1 L/min), heated from room temperature to 600 °C at 5 °C/min and held for 2 h. After cooling under continuous $N_2$ flow, the product was washed with 250 mL of 0.5 M HCl under ultrasonication for 10 min to remove residual inorganic species and unreacted activating agent, vacuum-filtered, and rinsed with deionised water until the filtrate reached neutral pH. The washed solid was dried at 105 °C for 30 min and stored in a desiccator. This sample is denoted PPC-NaOH; the untreated precursor is denoted PPC.

### 2.3 Oxidative Post-Treatment

For $H_2O_2$ treatment, PPC-NaOH was dispersed in 100 mL of 30% $H_2O_2$ and ultrasonicated for 2 h. The suspension was vacuum-filtered, and the solid was washed three times with 100 mL of deionised water per cycle and dried at 80 °C for 1 h, yielding PPC-NaOH-$H_2O_2$.

For AP treatment, PPC-NaOH was dispersed in 50 mL of 2 M $H_2SO_4$, and 50 mL of 1 M $(NH_4)_2S_2O_8$ was added dropwise with stirring. The mixture was ultrasonicated for 2 h, vacuum-filtered, washed three times with 100 mL of deionised water, and dried at 80 °C for 1 h, yielding PPC-NaOH-AP.

Each route was applied under the conditions conventional for its oxidant rather than under conditions matched between the two. They differ in oxidant concentration, in reaction medium and in redox potential: the AP route is carried out in 2 M $H_2SO_4$ and the $H_2O_2$ route in water, and neither product received an acid wash after oxidation. The comparison drawn in this work is therefore between two treatments as they are commonly practised, not between two oxidants at equal strength, and it does not rank them. Demineralisation and sulfur retention are attributed throughout to the AP route as practised, not to the persulfate ion: without an acid-only control, neither can be partitioned between the oxidant and its medium (Sections 3.5 and 3.8). The full preparation route is shown in Figure 1.

### 2.4 Characterisation

Crystalline phases were identified by X-ray diffraction (XRD, SmartLab, Rigaku) with Cu K$\alpha$ radiation ($\lambda$ = 1.5406 Å) over $2\theta$ = 5–80°. Phase fractions were quantified by Rietveld refinement (BGMN [42]) using a six-phase model (quartz, rutile, calcite, halite, muscovite 2M1 and hematite, each verified against its powder-diffraction card before inclusion) plus two broad Le Bail functions for the amorphous contribution. The PPC pattern [41] was refined here with the same model as the NaOH series. Fractions are reported on a crystalline basis only; no internal standard was added, so the absolute amorphous content is not quantified [43]. The refinement of PPC-NaOH did not yield usable fractions and is reported as rejected (Section 3.4). Surface functional groups were recorded by Fourier-transform infrared spectroscopy (FTIR, IRSpirit, Shimadzu) in attenuated total reflectance mode over 4000–400 $cm^{-1}$; spectra are displayed as transmittance, and band areas were computed on absorbance after convex-hull baseline correction. Morphology and local elemental composition were examined by field-emission scanning electron microscopy (FE-SEM, SU8000, Hitachi) with energy-dispersive X-ray spectroscopy (EDS, EMAX, Horiba); bulk inorganic composition was determined by energy-dispersive X-ray fluorescence (EDXRF, MESA-50, Horiba) at 15 kV and 200 µA using the fundamental parameter method. Thermal behaviour was measured by thermogravimetric analysis (TGA/DTG, DTG-60, Shimadzu) from room temperature to 800 °C at 10 °C/min under flowing air; the residue at 800 °C was taken as the ash content. Zeta potential was measured with a nanoparticle analyser (SZ-100, Horiba) at neutral pH with seven replicates per sample.

XRF and EDS both report weight percentages normalised to the quantified elements only, so leaching of one element raises the apparent content of all others, and neither technique reports the quantity of the mineral fraction. Element loadings were therefore obtained by scaling the XRF composition by the thermogravimetric ash content,

$$w_i = f_{\mathrm{ash}}\, c_i, \tag{1}$$

where $c_i$ is the XRF weight fraction of element $i$ and $f_{\mathrm{ash}}$ the ash fraction, giving grams of element per gram of product char. The scaling is semi-quantitative: XRF quantifies metals, chlorine and sulfur but not the oxygen, carbon or hydrogen that make up the remainder of the ash, so loadings are overestimated by a factor that varies with the phase assemblage. Changes between samples are therefore interpreted as fold-changes relative to the parent PPC-NaOH rather than as absolute inventories. Treatment yields were not recorded, so loadings are per gram of product and do not close a mass balance across the oxidation step. Sodium was not included in the EDS or XRF quantification lists and is not reported. It cannot be recovered from the raw EDS spectra, because Na K$\alpha$ (1.041 keV) lies within one detector resolution width of Zn L$\alpha$ and the Cu/Zn K lines are not excited at 15 kV.

### 2.5 Methylene Blue Adsorption

Batch experiments used 10 mg of adsorbent in 100 mL of MB solution ($V/m$ = 10 $L/g$), agitated at 150 rpm in a thermostatic

**Table 1.** Oxidative and alkali treatments of carbon adsorbents, and whether the inorganic fraction is quantified apart from the carbon. Ash values are as reported by each source; n.r. = not reported. Capacities are the maximum reported for the stated adsorbate, in mg $g^{-1}$ unless marked † (mmol $g^{-1}$) or ‡ (percentage removal). The final column records what each study measures, not the quality of its conclusions.

| Precursor (ash) | Activation | Oxidative or post-treatment | Characterisation axes | Adsorbate (capacity) | Inorganic fraction quantified separately? | Ref. |
|---|---|---|---|---|---|---|
| *Oxidative modification of carbons* | | | | | | |
| Commercial granular AC (n.r.) | none | AP in 1 M $H_2SO_4$ | BET, FTIR | Cr(VI) (108.7) | No: no ash, phase or elemental analysis | [25] |
| Pomegranate-peel biochar (n.r.) | none | $H_2O_2$; $HNO_3$ | BET, XRD, FTIR, TGA ($N_2$), XPS, EDS, $pH_{PZC}$ | Cu(II) (140.8) | No: TGA run for thermal stability; EDS "minor impurities" unquantified | [26] |
| Filtrasorb F-400 (0.1% after HF/HCl) | none | $HNO_3$; $H_2SO_4$; $O_3$ | BET, Boehm, TG, FTIR, SEM-EDX | nitrobenzene (5.11†) | **Yes**: deashed to 0.1%; ash removal raises uptake | [29] |
| *Alkali-activated and waste-polymer chars* | | | | | | |
| Mixed plastic pyrolysis char (n.r.) | NaOH | none | BET, XRD, ATR-FTIR, SEM, $pH_{PZC}$ | MB (68.7) | No: XRD peaks assigned to plastic pigments, not quantified | [16] |
| *Platanus*-seed hydrochar (n.r.) | NaOH | none | BET, XRPD, FTIR, FE-SEM, TG | none reported | No: silica identified by FTIR, XRD and SEM, never quantified | [13] |
| Tyre pyrolysis char (proximate on char) | KOH | none | XRD ($CaF_2$ standard), BET | none reported | No: Zn and K peaks noted; phases neither identified nor quantified | [38] |
| Municipal plastic-waste char (38.3%) | $K_2CO_3$ | none | proximate, $N_2$ sorption, SEM-EDS, trace elements | Pb(II) (35.5) | Partial: ash measured; capacity not normalised to it | [8] |
| Tea waste + metallised plastic (11.3–15.6% in char) | KOH | HCl wash | proximate, TGA, XRD, FTIR, FESEM, BET | MB (182.9) | Partial: ash on the chars only, not on the activated carbons | [39] |
| Sewage sludge (measured) | $H_2SO_4$ | HCl wash | ash, BET, XRD, TGA, FTIR, SEM-EDS, $pH_{PZC}$ | MB (98.9) | **Yes**: ash removal is the treatment variable | [30] |
| Spent tea leaves (n.r.) | none | none | zeta potential, XRD, FTIR, BET, SEM-EDS | MB (92‡) | No: surface charge carries the interpretation | [40] |
| *Fields in which the inorganic fraction is a routine variable* | | | | | | |
| Four lignocellulosic biomasses (0.14–7.65%) | none | water and acid washing | proximate, AAEM inventory, TGA, Raman | none (oxidation reactivity) | **Yes**: demineralisation rates reported per element | [31] |
| Ten coals (6.1–39.4%) | none | none | proximate, ultimate, petrography | $CO_2$ (0.78–2.17†) | **Yes**: reported on dry-ash-free and mineral-matter-free bases | [32] |
| NaOH-activated PPC (60.7%; 52.1% after $H_2O_2$, 16.8% after AP) | NaOH | $H_2O_2$; AP in 2 M $H_2SO_4$ | TGA (air), XRD with QPA, XRF, EDS, FTIR, zeta potential | MB (57.6 at 120 min) | **Yes**: ash-scaled element inventory; capacity also on an ash-free basis | This work |

shaker at 25 °C. Isotherms were measured at initial concentrations of 2, 5, 8 and 10 mg/L at the natural solution pH. The effect of pH was examined at pH 3, 7 and 11, adjusted with 0.1 M HCl or 0.1 M NaOH, at an initial concentration of 10 mg/L. Aliquots were withdrawn at intervals over 120 min, filtered through a 0.45 µm syringe filter, and the residual MB concentration was measured at $\lambda_{max}$ = 664 nm by UV–Vis spectrophotometry.

Uptake at time $t$ was calculated as

$$q_t = \frac{(C_0 - C_t)\,V}{m} \tag{2}$$

where $C_0$ and $C_t$ (mg/L) are the initial and time-dependent MB concentrations, $V$ (L) the solution volume and $m$ (g) the adsorbent mass.

#### 2.5.1 Initial Concentration Reference and Contact Time

In flasks where measurable depletion occurred before the first stable reading, the measured initial concentration underestimates $C_0$. A selective correction, $C_0 = \max(C_{0,measured}, C_{0,nominal})$, was applied. It raises $C_0$ only in those flasks and leaves the others at their measured value; 6 of the 12 flasks in this series were affected. The correction is one-sided: it can raise uptake but never lower it, and it assumes that the nomi-

nal concentration was prepared correctly. Uptake is therefore tabulated on both bases (Table 4). In the six affected flasks, the correction adds 0.3 to 11.5 mg/g (0.9 to 31% of the corrected value) and accounts for 21% of the fitted capacity of PPC-NaOH and 9% of that of PPC-NaOH-$H_2O_2$. Applying it improves the Langmuir fit, from $R^2$ = 0.63 to 0.96 and from 0.65 to 0.87, respectively.

Uptake did not reach a plateau within 120 min for any sample. In the pH series the fractional rise over the final interval, $(q_{120} - q_{90})/q_{120}$, was 5.8–7.4% for the oxidised chars. In the isotherm series, the distance from equilibrium is larger and varies with $C_0$: extrapolating each kinetic run to its pseudo-second-order plateau places $q_e$ up to 42% above the measured 120 min value, with the widest gaps in the 5 and 10 mg/L flasks.

All 120 min values are therefore reported as $q_{120}$, an uptake at fixed contact time, and never as equilibrium capacities. The Langmuir parameters fitted to them are correspondingly labelled $q_{m,120}$, an apparent capacity at that contact time. The extrapolated plateaus are tabulated flask by flask alongside the measured values (Table 4) so that the distance from equilibrium is visible at every point, but they are not themselves fitted: extrapolation makes the uptake of all three samples non-monotonic in $C_0$, which the Langmuir model does not admit. Isotherm parameters are reported only where uptake increased monotonically with $C_0$, as the model requires.

### 2.6 Kinetic and Isotherm Models

Kinetic data were fitted with the pseudo-first-order (PFO) and pseudo-second-order (PSO) models [44,45,46],

$$q_t = q_e \left(1 - e^{-k_1 t}\right) \tag{3}$$

$$q_t = \frac{k_2\, q_e^2\, t}{1 + k_2\, q_e\, t} \tag{4}$$

and with the Weber–Morris intraparticle diffusion model [47],

$$q_t = k_{id}\, t^{1/2} + C_i \tag{5}$$

where $k_{id}$ (mg/g min$^{-11/2}$) is the intraparticle diffusion rate constant and $C_i$ (mg/g) relates to the boundary-layer thickness. Weber–Morris plots were fitted as two-segment piecewise lines, with the breakpoint selected by least squares over all interior points with at least four points per segment. Isotherm data were fitted with the Langmuir model [48,49],

$$q_e = \frac{q_m\, K_L\, C_e}{1 + K_L\, C_e} \tag{6}$$

where $q_m$ (mg/g) is the monolayer capacity and $K_L$ (L/mg) the Langmuir constant. Because the uptake data are fixed-contact-time values rather than equilibrium values (Section 2.5.1), the fitted parameter is written $q_{m,120}$ throughout.

### 2.7 Replication

Zeta potential was measured with seven replicates per sample; it is the only axis on which a statistical test is possible. Differences between the two oxidised chars were assessed by equivalence testing rather than by a difference test, since failure to reject equality is not evidence of equivalence at this sample size. Two one-sided Welch tests were applied against an equivalence margin of ± 5 mV, declared before testing: the margin is approximately one standard deviation of either sample and lies inside the $|\zeta|$ = 30 mV boundary used to classify colloidal stability, so a difference smaller than the margin would not change how the surface charge is described. The Welch difference test, the Mann–Whitney test and Hedges' $g$ are also reported.

These measurements were made at the natural pH of the suspension. No potentiometric titration was performed, so neither a point of zero charge nor an isoelectric point was determined for these materials.

XRF, EDS, FTIR and TGA were each measured once per sample, so differences on those axes carry no error estimate, and no statistical test is applied to them.

## 3. RESULTS AND DISCUSSION

### 3.1 Surface Oxygen: The Two Oxidants Are Matched

Activation and oxidation each raise the surface oxygen content (Figure 2). The atomic O/C ratio from EDS rises from 0.220 in the raw char to 0.329 after NaOH activation, and each oxidative treatment raises it further, to 0.457 for $H_2O_2$ and 0.455 for AP. The two oxidised values differ by 0.002, so by this measure the oxidants are indistinguishable between single determinations: each adds the same ≈0.13 of atomic O/C to the activated char. Because EDS was run once per sample (Section 2.7), this is a comparison of individual measurements rather than distributions, and no significance is claimed for it. What it shows is that the two chars do not differ in surface oxygen, so the mineral-matrix differences reported in Section 3.4 cannot be attributed to such a difference.

This ratio does not, however, measure oxidation of the carbon surface specifically. In a solid that is 52–61 wt% ash (Section 3.3), most of the oxygen EDS detects is bound in the oxide, carbonate and silicate phases rather than in functional groups on carbon. Oxygen was assigned stoichiometrically to the mineral-forming elements reported by EDS between two end-members: metals in their lowest plausible oxides with sulfur carrying no oxygen, and metals in their highest plausible oxides with calcium as carbonate where calcite is detected and sulfur as sulfate. On that bracket, the mineral share is 85–98% of detected oxygen in PPC-NaOH-$H_2O_2$ and 56–87% in PPC-NaOH-AP. The share is large in both and differs between them. Subtracting it leaves carbon-associated O/C ranges too wide to distinguish the two chars, and for PPC and PPC-NaOH the same assignment requires more oxygen than EDS detects. No corrected ratio is therefore reported. The atomic O/C used here is the quantity conventionally reported for an oxidised char, and it takes the same value for two solids that the following sections show are not the same material.

The FTIR spectra give the same qualitative picture (Figure 2a). After either oxidation, the carbonyl/carboxyl band at 1780–1650 cm$^{-1}$ intensifies relative to the parent char [50,51], and the carbonate band at 1480–1380 cm$^{-1}$, prominent in PPC and PPC-NaOH, weakens markedly, consistent with the calcite depletion resolved by XRD (Section 3.4). ATR band intensities are not quantitative across samples that differ in contact and scattering, so these changes are interpreted as directions, not magnitudes. The strongest feature in both oxidised spectra, the envelope at 950–1200 cm$^{-1}$, belongs to the mineral Si–O–Si framework (shaded in Figure 2a); silicon varies threefold across the series, and the band therefore carries no information about carbon–oxygen chemistry.

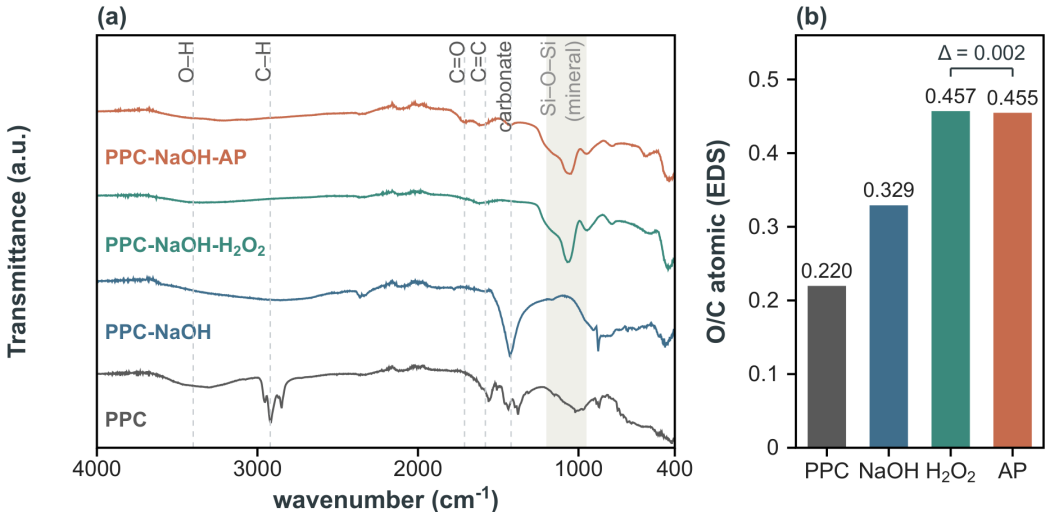


**Figure 2.** Surface chemistry of the NaOH series. (a) ATR-FTIR spectra (transmittance, normalised per spectrum, offset for clarity). Dashed guides mark the O–H, C–H, C=O, C=C and carbonate bands; the shaded window (950–1200 $cm^{-1}$) is the mineral Si–O–Si envelope and is not read as carbon oxidation. Band areas quoted in the text are computed on baseline-corrected absorbance (Section 2.4). (b) Atomic O/C from EDS (O 15.999, C 12.011); values are single determinations, so no error bars are shown.

### 3.2 Surface Charge: The Two Oxidants Are Matched

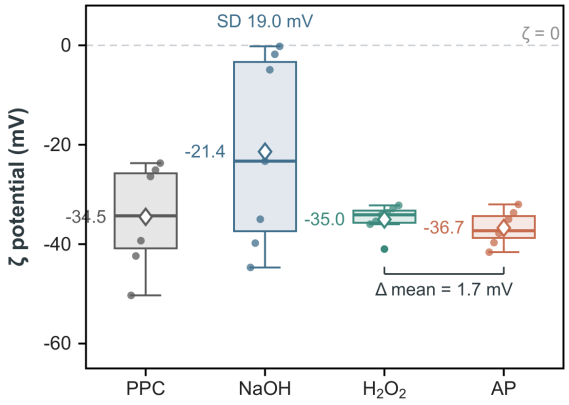


**Figure 3.** Zeta potential at neutral pH. Boxes mark the median and interquartile range with Tukey whiskers; dots are the seven individual replicates per sample and open diamonds the means quoted in the text. The dashed line marks zero charge. The bracket ties the two oxidised samples, whose means differ by 1.7 mV.

Zeta potential separates the activation step from the oxidation steps (Figure 3). The raw char sits at $-34.5 \pm 10.0$ mV at neutral pH (mean $\pm$ SD, $n = 7$). Activation does not so much shift this distribution as broaden it: the seven PPC-NaOH replicates span $-44.7$ to $-0.2$ mV (SD 19.0 mV), so the mean of $-21.4$ mV describes no single population. The spread is itself the observation: after activation, surface charge is heterogeneous on the scale sampled by individual replicate measurements [52,53].

Either oxidation collapses that heterogeneity onto the same value. The $H_2O_2$-treated char measures $-35.0 \pm 3.0$ mV and the AP-treated char $-36.7 \pm 3.4$ mV, and the spreads narrow about six-fold relative to PPC-NaOH. The two are equivalent within $\pm$ 5 mV: the difference is 1.70 mV with a 90% confidence interval of $-1.33$ to +4.73 mV, and both one-sided tests reject non-equivalence ($p = 0.0010$ and $p = 0.038$). The difference tests do not resolve them either (Welch $t = 1.00$, $p = 0.34$; Mann–Whitney $p = 0.41$; Hedges' $g = 0.50$, 95% CI $-0.57$ to +1.57), though that on its own would not establish equivalence. The equivalence criterion is met narrowly: the upper confidence limit reaches 4.73 mV against the 5 mV bound. By the second descriptor conventionally used to characterise an oxidised carbon surface, the two oxidants are equivalent at a resolution finer than any distinction the descriptor is used to draw.

To this point the two treatments appear interchangeable. The sections that follow show they are not: what separates them lies in the inorganic matrix of the char (Sections 3.3 and 3.4), not on its carbon surface.

### 3.3 Ash Content: The Two Oxidants Separate

The residue after combustion gives the first quantitative separation of the two oxidants (Figure 4). The raw char leaves 41.5 wt% ash. Activation raises this to 60.7 wt%, as expected for a step that consumes carbon at 600 °C and removes soluble matter in the wash, concentrating the minerals left behind. It is on this ash-dominated solid that the two oxidants act, and here they no longer act alike. $H_2O_2$ treatment lowers the ash content by 8.6 percentage points, to 52.1 wt%; AP treatment removes most of the mineral load outright, leaving 16.8 wt%. Under the same contact time, temperature and washing (Section 2.3), one oxidant leaves an ash-rich solid and the other converts the char into a carbon-dominated one.

Elemental analysis resolves the same separation element by element (Table 2). Because XRF is normalised to its quantified elements, its weight percentages describe the composition of the mineral fraction and not its quantity: calcium, for instance, holds nearly constant at 6.7 and 6.5 wt% of quantified elements between PPC-NaOH and PPC-NaOH-AP, which would suggest it survives the treatment. Scaling by ash content (Equation (1)) shows it does not. Relative to the activated char, the AP route removes 88% of the potassium, 73% of the calcium and iron and 67% of the silicon; calcium falls from 4.08 to 1.10 g per 100 g of product. The $H_2O_2$ route

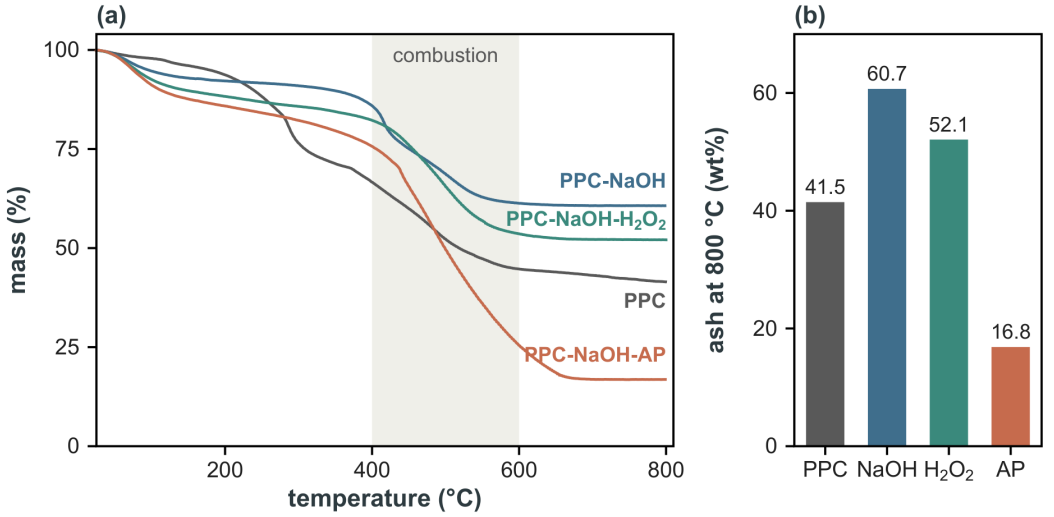


**Figure 4.** Thermogravimetry in air. (a) Mass-loss curves; the shaded window (400–600 °C) is the carbon combustion regime. (b) Residue at 800 °C, taken as ash content. Each curve is a single thermogram.

**Table 2.** Elemental composition and ash-scaled loading of the NaOH series by XRF. Composition is normalised to the quantified elements, so it describes the mineral fraction and not its quantity; loading is that composition scaled by the ash content of Figure 4 (Equation (1)) and is comparable between samples. The last two columns are loadings relative to the activated char. Al, Cr, Cu, Mn, Ni, V and Zn together account for 1.06, 0.43 and 1.23 wt% of quantified elements and are omitted. Each value is a single determination.

| | Composition (wt%) | | | Loading (g/100 g) | | | Relative to NaOH | |
|---|---|---|---|---|---|---|---|---|
| | NaOH | $H_2O_2$ | AP | NaOH | $H_2O_2$ | AP | $H_2O_2$ | AP |
| Ti | 41.92 | 50.24 | 19.55 | 25.45 | 26.17 | 3.29 | 1.03 | 0.13 |
| Si | 35.04 | 33.12 | 42.23 | 21.27 | 17.25 | 7.12 | 0.81 | 0.33 |
| Fe | 10.44 | 11.49 | 10.11 | 6.34 | 5.99 | 1.70 | 0.94 | 0.27 |
| Ca | 6.72 | 3.47 | 6.54 | 4.08 | 1.81 | 1.10 | 0.44 | 0.27 |
| K | 3.67 | 0.39 | 1.57 | 2.23 | 0.20 | 0.26 | 0.09 | 0.12 |
| Cl | 0.95 | 0.77 | 7.53 | 0.58 | 0.40 | 1.27 | 0.70 | 2.19 |
| S | 0.19 | 0.09 | 11.25 | 0.12 | 0.04 | 1.89 | 0.38 | 16.20 |
| Ash (wt%) | | | | 60.7 | 52.1 | 16.8 | 0.86 | 0.28 |

removes 0 to 56% of the same elements. Depletion on the AP route is thus broad rather than selective: every major mineral element loses between two-thirds and nine-tenths of its loading. This is the pattern expected from an acidic medium acting on a mixed assemblage rather than from oxidative attack on a single phase.

Titanium is depleted along with the rest, and more than proportionately: its loading falls by 87% compared with 72% for the ash as a whole. It is therefore not a conserved reference in this series, and ratios normalised to it would overstate the enrichment of anything measured against it. Diffraction agrees in direction: rutile falls from the dominant crystalline phase after $H_2O_2$ treatment to a trace over the amorphous hump after AP treatment (Table 3). All elemental comparisons in this work are therefore made on the ash-scaled basis.

The shape of the mass-loss curves is consistent with this. In the combustion window (400–600 °C), the AP-treated char loses 50.2% of its initial mass, compared with 24.7% for PPC-NaOH and 28.6% for the $H_2O_2$-treated char, so combustible carbon is now its majority component. These are single thermograms, so the comparisons are between individual runs. The same ordering is, however, obtained independently from the diffraction results that follow (Section 3.4), which resolve the mineral loss phase by phase.

### 3.4 Crystalline Phases: The Two Oxidants Separate

The parent char carries a crystalline assemblage of quartz, rutile, calcite, halite and muscovite (Figure 5a,c). Rietveld refinement of the six-phase model converged at $R_{wp}$ = 12.5% and distributed the crystalline fraction as 30.4 wt% quartz, 31.8 wt% rutile, 23.9 wt% calcite, 8.3 wt% halite and 5.5 wt% muscovite (Table 3). A weak hematite reflection at 33.0° passes card verification in this pattern, but the phase refines to zero; across the series, hematite never exceeds 2.6 wt% where it refines to a stable fraction. These fractions are relative to the crystalline part only: without an internal standard, neither the carbon nor any glassy silicate is quantified. Anatase is absent from all four patterns, and crystalline titanium occurs only as rutile.

Activation removes halite, as expected from the wash to neutral filtrate, and depletes calcite: the calcite 104 reflection at 29.4°, among the strongest lines of the parent pattern, falls below detection in PPC-NaOH (Figure 5b). The PPC-NaOH pattern itself, however, does not support quantification. Its mica 002 reflection at 8.85° is narrower than every other reflection in the same scan (FWHM 0.060° against 0.110° for quartz) and its basal-to-non-basal intensity ratio departs from the powder value by more than an order of magnitude, which is the signature of a coarse, basally oriented flake rather than of mica content. Two further sharp reflections, at 10.54° and 28.06° ($d$ = 8.39 and 3.18 Å), match none of the candidate phases. With the dominant reflection an artefact of particle statistics and two others unassigned, the refinement converged only at $R_{wp}$ = 22.8% (Figure 5d), and its fractions were rejected rather than reported.

The two oxidised chars separate (Figure 5e,f). After $H_2O_2$ treatment, the parent assemblage survives: quartz, rutile and muscovite persist at 31.2, 52.7 and 8.6 wt%, with residual calcite at 4.8 wt% ($R_{wp}$ = 13.2%). After AP treatment, the crystalline remainder is reduced to two trace phases, quartz and rutile (84.6 and 15.4 wt% of what little remains), on a

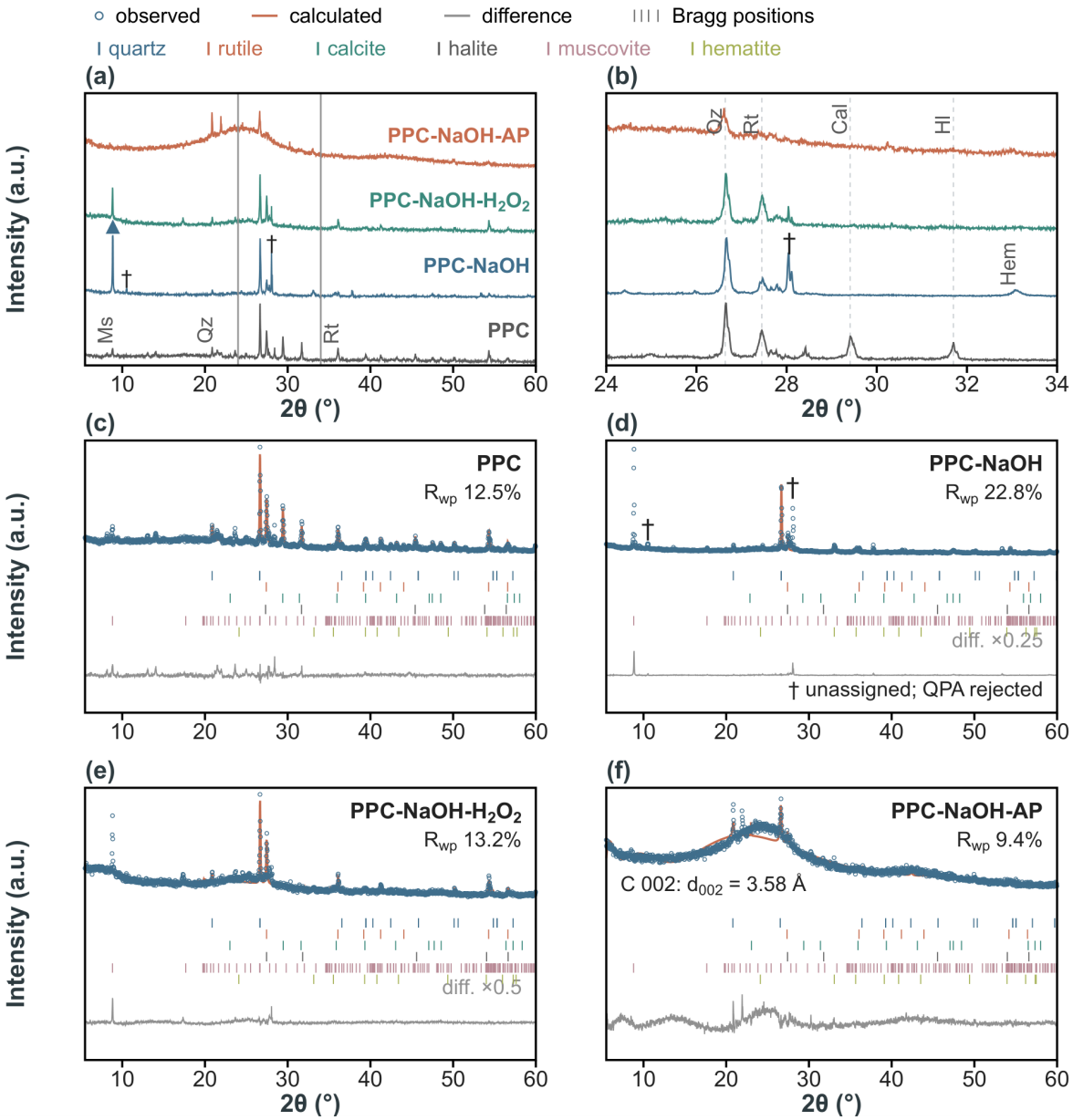


**Figure 5.** XRD of the NaOH series. (a) The four patterns, bottom to top as labelled; grey rules bracket the window enlarged in (b). The PPC-NaOH trace is normalised to its quartz 26.66° reflection; its mica 002 reflection at 8.85° (▲) is clipped, and † marks two reflections (10.54°, 28.06°) matching no candidate phase. Ms = muscovite, Qz = quartz, Rt = rutile. (b) The 24–34° window; dashed guides mark quartz, rutile, calcite (Cal) and halite (Hl); Hem = hematite. (c–f) Rietveld fits (BGMN): observed points, calculated curve, difference (scaled where indicated) and Bragg positions coloured by phase as keyed above. $R_{wp}$ per panel; the phase fractions of (d) are rejected (see text). PPC pattern first reported in [41].

**Table 3.** Rietveld phase fractions (wt%, crystalline basis) for the NaOH series. Uncertainties are 1$\sigma$ estimates from BGMN. The amorphous fraction is not quantified (no internal standard). The PPC-NaOH refinement is rejected and its fractions are not reported (see text).

| Sample | $R_{wp}$ (%) | Quartz | Calcite | Rutile | Halite | Muscovite | Hematite |
|---|---|---|---|---|---|---|---|
| PPC | 12.5 | 30.4 ± 0.7 | 23.9 ± 0.6 | 31.8 ± 0.6 | 8.3 ± 0.2 | 5.5 ± 0.6 | 0 |
| PPC-NaOH | 22.8 | — | — | — | — | — | — |
| PPC-NaOH-$H_2O_2$ | 13.2 | 31.2 ± 1.3 | 4.8 ± 0.8 | 52.7 ± 1.4 | 0 | 8.6 ± 1.0 | 2.6 ± 0.7 |
| PPC-NaOH-AP | 9.4 | 84.6 ± 1.7 | 0 | 15.4 ± 1.7 | 0 | 0 | 0 |

broad amorphous band; calcite, muscovite and hematite are below detection. Under the same contact time, temperature and washing, one oxidant leaves the mineral assemblage of the char intact and the other strips it to traces.

The routes differ in their medium as well as their oxidant, and the phase-by-phase pattern follows the medium at least as closely as the oxidant. Calcite is the phase lost most completely, and carbonate dissolves in 2 M $H_2SO_4$ without any oxidant, so its disappearance on the AP route does not require persulfate. Muscovite, the next most acid-susceptible phase of the assemblage, is likewise undetected, while quartz and rutile, the two most resistant, survive. Neither the ordering of the phases nor the breadth of the elemental depletion (Section 3.3) distinguishes the acid from the oxidant, and no acid-only control was run. Demineralisation is therefore reported as a property of the AP route as practised (Sections 2.3 and 3.8).

Loss of the calcite reflections does not by itself show that the calcium has dissolved. In a carbonate-bearing sludge char, activation with $H_2SO_4$ converts $CaCO_3$ to $CaSO_4$ rather than dissolving it [30], which removes the calcite reflections while the calcium stays in the solid. That is not what happens here: no gypsum or anhydrite reflection appears in the AP pattern, and the ash-scaled inventory places the calcium loading 73% below that of the activated char (Section 3.3), so the calcium leaves the solid rather than changing phase within it.

The band that dominates the PPC-NaOH-AP pattern is centred at 24.5–25.5°, corresponding to $d_{002}$ = 3.58 ± 0.07 Å, and is accompanied by a weaker two-dimensional (10) band near 42°. Together, the two bands are the signature of turbostratic carbon [54,55]. The band position argues against silica glass, whose halo falls at 21.5–22.5° [56], roughly 3° below the observed centre, and silica glass produces no counterpart to the 42° band. The band amplitude also rises across the series as the ash content (Section 3.3) falls, the opposite of what a silicate glass would produce. A minor sodium-silicate contribution nevertheless cannot be excluded on XRD evidence alone. The interlayer spacing, some 7% wider than that of graphite (3.354 Å), is consistent with turbostratic stacking disorder and falls within the 3.58–3.66 Å range reported for non-graphitising activated carbons prepared from tyre pyrolysis char [38]. Because the quartz–rutile–calcite cluster at 26–30° overlies the 002 window in every other sample, $d_{002}$ is reported for PPC-NaOH-AP only.

### 3.5 Sulfur Retention

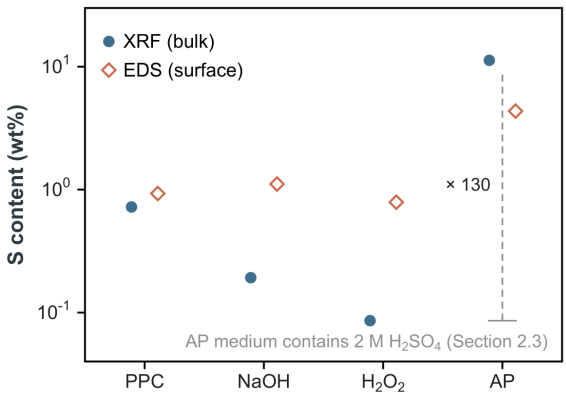


**Figure 6.** Sulfur content across the NaOH series by XRF (bulk, filled circles) and EDS (surface, open diamonds); note the logarithmic scale. Each value is a single determination. The dashed riser marks the ratio between the $H_2O_2$ and AP branches of the bulk series.

Sulfur enters the char through the AP route alone (Figure 6). The native sulfur of the raw char (0.72 wt% by XRF) is largely removed by activation and washing (0.19 wt% in PPC-NaOH, 0.09 wt% after $H_2O_2$ treatment). The AP-treated char instead carries 11.25 wt%, two orders of magnitude more than its $H_2O_2$ counterpart. EDS shows the same direction at the surface (4.35 against 0.79 wt%). The two techniques disagree in magnitude because each normalises to its own quantified element set (Section 2.4), but they agree in direction and rank. Scaled by ash content (Equation (1)), the sulfur loading rises sixteen-fold from the activated char to the AP-treated char, from 0.12 to 1.89 g per 100 g of product.

The retained sulfur is amorphous to X-rays. The PPC-NaOH-AP pattern contains no reflection of thenardite, aphthitalite, arcanite or elemental $S_8$ (Section 3.4), which excludes crystalline sulfate salts. Given that the same sample retains almost no crystalline mineral of any kind, the sulfur most likely resides in or on the carbon-rich solid rather than in a discrete salt phase.

The present data cannot, however, assign that sulfur to the oxidant. The AP oxidation is carried out in 2 M $H_2SO_4$ and the product receives only a water wash (Section 2.3), so the retained sulfur has two candidate origins (sulfonate grafted during persulfate oxidation [25] or sulfate adsorbed from the acid medium), and nothing in this dataset separates them. The discriminating measurement is XPS S 2p, where sulfonate appears near 168 eV and adsorbed sulfate at 169–170 eV [57,58]; it was not performed here. The finding is therefore reported without assignment: the AP route leaves the char with about 11 wt% sulfur on a bulk basis, and its speciation remains unresolved.

### 3.6 Methylene Blue Uptake

The raw char takes up less than 4 mg/g of MB; every treated char exceeds it by an order of magnitude. At $C_0$ = 10 mg/$L$ and natural pH (Figure 7a), the 120-min uptakes rank $H_2O_2$ (46.5) > NaOH (37.2) > AP (33.5 mg/g), but this ranking does not describe equilibrium. The pseudo-second-order model describes all three series, and its extrapolated capacities reorder the bottom of the list: 56.5, 37.1 and 47.5 mg/g, respectively. The AP-treated char is the furthest from equilibrium at 120 min (extrapolated $q_e$ 42% above the 120-min value, compared with 21% for $H_2O_2$ and <1% for PPC-NaOH), so fixed-time uptake understates it most.

Langmuir fits of the 120-min isotherms (Figure 7b, Table 4) give an apparent capacity $q_{m,120}$ = 44.7 mg/$g$ ($K_L$ = 1.06, $R^2$ = 0.955) for PPC-NaOH and 57.6 mg/g ($K_L$ = 0.66, $R^2$ = 0.866) for PPC-NaOH-$H_2O_2$, a 29% gain from the $H_2O_2$ step on a per-gram basis at fixed contact time. Two qualifications bound that number, and both work in the same direction.

The first is the contact time. All but one flask in Table 4 sit below their pseudo-second-order plateaus, which lie up to 42% above the measured values, and for the oxidised chars the gap is largest in the 5 and 10 mg/L flasks. The fitted values are therefore apparent capacities, not monolayer capacities.

The second is the basis. Ash accounts for 60.7 wt% of PPC-NaOH and 52.1 wt% of PPC-NaOH-$H_2O_2$ (Section 3.3), so a gram of each contains 0.39 and 0.48 g of non-mineral material, and the per-gram comparison is between unlike quantities. On an ash-free basis the same two fits give 113.7 and 120.2 mg/g, a gain of 6% rather than 29%. Most of the per-gram improvement from the $H_2O_2$ step is therefore the removal of mineral diluent. Per unit mass, the non-ash fraction of the oxidised char binds methylene blue at close to the

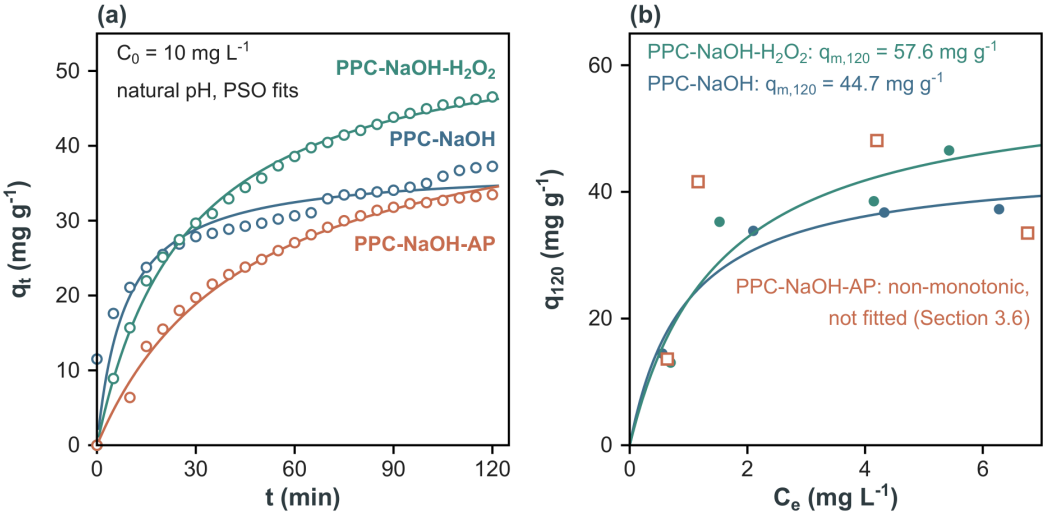


**Figure 7.** MB uptake at natural pH, $C_0$-corrected. (a) Kinetics at $C_0$ = 10 mg/$L$: points are measured $q_t$, curves are PSO fits. (b) 120-min isotherms with Langmuir fits for PPC-NaOH and PPC-NaOH-$H_2O_2$; the PPC-NaOH-AP series (open squares) is non-monotonic and is shown without a fit.

same capacity as that of the activated char before oxidation. The direction is not particular to this series: demineralising a commercial activated carbon to 0.1 wt% ash raises its measured uptake, an increase attributed to reopening micropores that the mineral fraction had blocked [29]. The magnitudes are not comparable: that material was taken to near-zero ash, whereas these chars retain 52–61 wt%. In both cases, however, the ash content must be known before a per-gram capacity can be interpreted as a property of the carbon. The ash-free basis is not a carbon basis: the non-ash fraction is organic matter and moisture, and no elemental carbon determination was made on this series.

On a per-gram basis, these capacities fall where a filler-derived char would be expected to fall: an order of magnitude below optimised high-surface-area activated carbons, whose MB capacities reach 325–1000 mg/g [59,60,61], and of the same order as unactivated biochar and reduced graphene oxide [62,63]. The observation of interest is not the absolute capacity but the contrast between the two oxidative routes on the same activated char. For PPC-NaOH-AP, the four-point series is non-monotonic (13.6, 41.6, 48.1, then 33.5 mg/g at the highest $C_0$), which violates the premise of the Langmuir model, so no isotherm parameter is extracted. The kinetics offer a partial explanation: the 10 mg/L flask is the one furthest from equilibrium, and its extrapolated $q_e$ of 47.5 mg/g would restore near-monotonicity. Extrapolation cannot substitute for a longer run, however, and the capacity of this sample is left unquantified. Nor does extrapolation help the other two series: on the plateau values of Table 4, all three samples become non-monotonic in $C_0$, so no Langmuir parameter is fitted to the plateaus.

### 3.7 pH Response

The two oxidised chars respond to pH with different shapes, not merely different sizes (Figure 8a,b). At 120 min, PPC-NaOH-AP peaks at pH 7 (36.8, 56.0, 50.9 mg/g at pH 3, 7, 11), while PPC-NaOH-$H_2O_2$ rises monotonically and six-fold across the same range (7.7, 26.2, 48.4 mg/g), the electrostatic pattern expected for a cationic adsorbate [24].

Because not every run had reached a plateau at 120 min,

**Table 4.** MB uptake of the NaOH series at natural pH and 120 min contact. $q_{120}$ is given on the uncorrected and $C_0$-corrected bases (Section 2.5.1); $q_e^{PSO}$ is the pseudo-second-order plateau extrapolated from the 25-point kinetic series of that flask, and Δ its excess over the corrected $q_{120}$. Ash-free values divide the corrected $q_{120}$ by the non-ash fraction. All $q$ values are in mg/g. All entries are single determinations.

| Sample | $C_0$ (mg/L) | $C_e$ | $q_{120}$ uncorr. | $q_{120}$ corr. | $q_e^{PSO}$ | Δ (%) | $q_{120}$ ash-free |
|---|---|---|---|---|---|---|---|
| PPC-NaOH | 2.00 | 0.55 | 12.4 | 14.5 | 15.3 | 5.5 | 36.8 |
| | 5.49 | 2.10 | 33.9 | 33.9 | 39.7 | 17.3 | 86.1 |
| | 8.00 | 4.33 | 36.4 | 36.7 | 39.7 | 8.1 | 93.4 |
| | 10.00 | 6.28 | 25.7 | 37.2 | 37.1 | −0.4 | 94.8 |
| PPC-NaOH-$H_2O_2$ | 2.00 | 0.70 | 9.7 | 13.0 | 13.4 | 3.0 | 27.2 |
| | 5.05 | 1.52 | 35.3 | 35.3 | 47.6 | 35.0 | 73.6 |
| | 8.00 | 4.15 | 28.6 | 38.5 | 44.5 | 15.4 | 80.4 |
| | 10.08 | 5.43 | 46.5 | 46.5 | 56.5 | 21.4 | 97.2 |
| PPC-NaOH-AP | 2.00 | 0.64 | 12.2 | 13.6 | 14.0 | 2.5 | 16.4 |
| | 5.32 | 1.16 | 41.6 | 41.6 | 54.7 | 31.4 | 50.0 |
| | 9.01 | 4.20 | 48.1 | 48.1 | 52.7 | 9.6 | 57.8 |
| | 10.11 | 6.76 | 33.5 | 33.5 | 47.5 | 42.0 | 40.3 |
| *Langmuir fitted to the corrected $q_{120}$* | | | | | | | |
| PPC-NaOH | $q_{m,120}$ = 44.7 (36.8 uncorrected) | | | | $K_L$ = 1.06, $R^2$ = 0.955 | | 113.7 |
| PPC-NaOH-$H_2O_2$ | $q_{m,120}$ = 57.6 (52.6 uncorrected) | | | | $K_L$ = 0.66, $R^2$ = 0.866 | | 120.2 |
| PPC-NaOH-AP | not fitted (uptake non-monotonic in $C_0$) | | | | | | |

**Table 5.** Kinetic parameters of the pH runs ($C_0$ = 10 mg/$L$, 120 min). PSO: $q_e$, $k_2$ (g mg$^{-1}$ min$^{-1}$); Weber–Morris two-segment fit: $k_{id,1/2}$ (mg/g min$^{-11/2}$), breakpoint $t_b$ (min).

| Sample | pH | $q_{120}$ | $q_e^{PSO}$ | $k_2$ | $R^2_{PSO}$ | $k_{id,1}$ | $k_{id,2}$ | $t_b$ | $R^2_{WM}$ |
|---|---|---|---|---|---|---|---|---|---|
| PPC-NaOH-$H_2O_2$ | 3 | 7.7 | 8.0 | 0.011 | 0.969 | 1.1 | 0.4 | 20 | 0.992 |
| | 7 | 26.2 | 29.7 | 0.002 | 0.986 | 3.3 | 1.7 | 25 | 0.998 |
| | 11 | 48.4 | 55.3 | 0.002 | 0.975 | 8.1 | 0.0 | 35 | 0.991 |
| PPC-NaOH-AP | 3 | 36.8 | 38.9 | 0.003 | 0.997 | 6.1 | 1.5 | 20 | 0.996 |
| | 7 | 56.0 | 64.7 | 0.001 | 0.985 | 6.6 | 3.9 | 25 | 0.997 |
| | 11 | 50.9 | 52.9 | 0.008 | 0.992 | 10.4 | 0.7 | 20 | 0.939 |

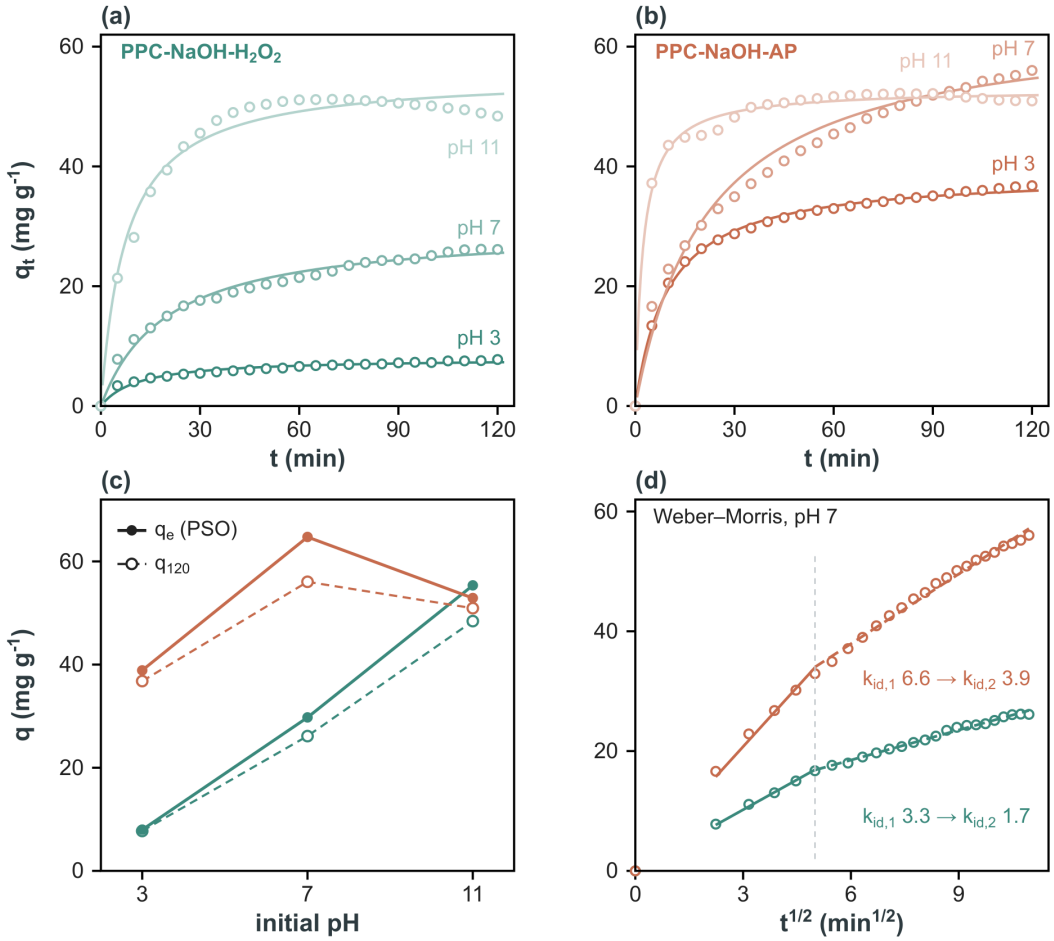


**Figure 8.** pH response of the oxidised chars at $C_0$ = 10 mg/$L$. (a, b) $q_t$ at initial pH 3, 7 and 11 (darker = lower pH) with PSO fits. (c) Uptake against pH: open symbols and dashed lines are measured $q_{120}$, filled symbols and solid lines the PSO-extrapolated $q_e$. (d) Weber–Morris plots of the two pH 7 runs with two-segment fits (solid/dashed = first/second segment; the dotted vertical lines mark the breakpoints); $k_{id}$ in mg/g $min^{-11/2}$.

part of this contrast could in principle reflect rate rather than affinity. The kinetic fits constrain that possibility (Table 5). Three runs sit furthest from equilibrium, both pH-7 runs and the $H_2O_2$ run at pH 11 (PSO-extrapolated $q_e$ 14–16% above $q_{120}$), and the other three lie within 3–6%. Extrapolating every run to its PSO plateau preserves both shapes (Figure 8c): the $H_2O_2$ response stays monotonic (8.0 → 29.7 → 55.3 mg/g) and the AP response stays peaked (38.9 → 64.7 → 52.9 mg/g). The point most exposed to this kinetic objection, the low $H_2O_2$ uptake at pH 3, is in fact the best-equilibrated run of the six ($q_e$ within 3% of $q_{120}$, with the largest rate constant): that char takes up little MB at pH 3 because its capacity there is small, not because it is slow. Model extrapolation is not a substitute for longer contact times, and runs to plateau would settle the question. Within the data at hand, however, the shape difference survives the correction.

Ash dilution accounts for part of the size difference but not for the shapes. On an ash-free basis the $H_2O_2$ response is still monotonic (16.2, 54.6, 101.0 mg/g at pH 3, 7 and 11) and the AP response still peaked at pH 7 (44.2, 67.4, 61.2 mg/g); the AP-to-$H_2O_2$ ratio falls from 4.75, 2.14 and 1.05 to 2.74, 1.23 and 0.61, so at pH 11 the ranking reverses. Which char takes up more therefore depends on the basis chosen and on the pH; the difference in shape does not.

The mechanistic reading of these shapes is bounded by what was measured. Both chars are strongly negative at neutral pH, where a cationic dye is therefore electrostatically favoured. The zeta potential was, however, measured at a single pH rather than titrated (Section 2.7), so no point of zero charge is available and the pH at which either surface would change sign is unknown. Electrokinetic and titrimetric quantities report different properties, and a zeta potential measured at one pH substitutes for neither [64,65]. Within that limit, the monotonic $H_2O_2$ response is what protonation of surface oxygen groups at low pH and their deprotonation at high pH would produce. The AP maximum at pH 7 instead requires a contribution that declines at pH 11, such as competition from the $Na^+$ introduced with the adjusting base, or dissolution and reprecipitation of residual mineral phases at the pH extremes, to which the two chars are not equally exposed. Distinguishing between these would require a titration and an ionic-strength series, neither of which was performed.

The Weber–Morris analysis (Figure 8d) separates the transport stages. Every run shows two stages, a fast initial segment breaking to a slower one at 20–35 min, and a single-line fit is clearly inferior (e.g. $R^2$ = 0.54 against 0.94 for PPC-NaOH-AP at pH 11). The intercepts are non-zero, indicating a boundary-layer contribution throughout. At pH 7, the AP-treated char diffuses faster than its $H_2O_2$ counterpart in both stages ($k_{id,1}$ = 6.6 against 3.3, $k_{id,2}$ = 3.9 against

1.7 mg/g $min^{-11/2}$), consistent with faster internal transport in the carbon-dominated, demineralised solid, although without textural data (Section 3.8) this interpretation remains kinetic rather than structural. The two chars enter these experiments with the same surface charge (Section 3.2). The pH response is where their difference first appears in application, and the matrix-level contrast of Sections 3.3 and 3.4 is the property that distinguishes them.

### 3.8 What the Surface Descriptors Miss

By the two descriptors conventionally used to characterise an oxidised carbon, the two treatments are interchangeable: atomic O/C of 0.457 against 0.455 (Section 3.1), zeta potential of $-35.0 \pm 3.0$ against $-36.7 \pm 3.4$ mV (Section 3.2). Yet the solids they leave behind are not the same material. One is half mineral (52.1 wt% ash) and retains the quartz–rutile–calcite–muscovite assemblage of its parent; the other is carbon-dominated (16.8 wt% ash), retains only traces of quartz and rutile over a turbostratic hump, and carries 11 wt% of X-ray-amorphous sulfur (Sections 3.3–3.5). The difference between the two products is larger than anything either surface descriptor registers.

This failure is structural rather than accidental. Both descriptors interrogate the carbon surface: O/C reports its composition, zeta potential the charge it presents to solution. In PPC-NaOH, which is 60.7 wt% ash, that surface belongs to the minority component, so two treatments can act very differently on most of the solid and still give the same values of both descriptors, as the AP and $H_2O_2$ treatments did. The consequences appear in application: two chars whose surface charge is equivalent within 5 mV respond to pH with different shapes (Figure 8c), and the intraparticle diffusion rate constants of the demineralised char are roughly twice those of its $H_2O_2$ counterpart in both Weber–Morris stages at pH 7 (Table 5).

The matrix also accounts for capacity that would otherwise be read as surface chemistry. The 29% rise in apparent Langmuir capacity from PPC-NaOH to PPC-NaOH-$H_2O_2$ falls to 6% once both are expressed per gram of ash-free material (Table 4): most of that gain is the removal of mineral diluent rather than an improvement in the non-mineral fraction. An uptake measured per gram of adsorbent inherits the ash content of whatever produced it.

Three limitations bound this reading. First, the textural link is unmeasured: removing 44 percentage points of ash from a solid would plausibly open porosity, and the faster intraparticle diffusion of the AP-treated char points the same way, but no surface-area or porosimetry measurement was made on this series, so the diffusion contrast is reported as kinetics and no textural claim is made. Second, the route-level caveat of Section 2.3 applies to the matrix as it does to the sulfur: the AP treatment differs from the $H_2O_2$ treatment in its 2 M $H_2SO_4$ medium as well as its oxidant, so the demineralisation belongs to the treatment as practised, not to the persulfate ion alone. An acid-only control, elemental analysis of the treatment filtrates (for example by ICP-OES) and a comparison at matched oxidant strength would partition the effect between oxidant and medium. None was performed, and the filtrates were not retained. Third, the surface chemistry is characterised by elemental ratio and by charge, not by speciation: no X-ray photoelectron spectra were recorded, so the functional groups behind the O/C parity are not resolved, and equal O/C does not establish that the two carbon surfaces carry the same functionality. Likewise, uptake was probed with a single cationic dye at 2–10 mg/L, which does not establish behaviour toward anionic, neutral or larger organic adsorbates. None of the three affects the methodological point. For a char whose inorganic fraction approaches or exceeds half its mass, the two standard surface descriptors together failed to register the largest change an oxidative treatment produced. Characterising such a treatment therefore requires a measurement of the mineral matrix alongside the surface chemistry, for which an ash determination and phase-resolved diffraction suffice. Reporting O/C alone leaves the larger structural change unrecorded.

## 4. CONCLUSIONS

NaOH-activated plastic pyrolytic char was treated with $H_2O_2$ or ammonium persulfate, and the carbon surface and the mineral matrix were characterised independently. On the surface axis the two oxidants are matched: atomic O/C reaches 0.457 and 0.455, and the zeta potential $-35.0 \pm 3.0$ and $-36.7 \pm 3.4$ mV ($n = 7$). On the matrix axis they separate. $H_2O_2$ treatment leaves the ash content at 52.1 wt% and the parent quartz–rutile–calcite–muscovite assemblage intact. The persulfate treatment reduces the ash to 16.8 wt% and the crystalline assemblage to traces of quartz and rutile over a turbostratic carbon hump ($d_{002} = 3.58 \pm 0.07$ Å), and leaves the solid carrying 11.25 wt% sulfur of unresolved speciation. The divergence extends to application, where the matrix again accounts for the result: $H_2O_2$ treatment raises the apparent MB capacity of the activated char from 44.7 to 57.6 mg/g at fixed contact time, but only from 113.7 to 120.2 mg/g once expressed per gram of ash-free material, so most of the per-gram gain reflects the loss of mineral diluent. The two oxidised chars respond to pH with differently shaped profiles, monotonic for $H_2O_2$ and peaked at pH 7 for AP, and this contrast survives both extrapolation of the unequilibrated runs to their kinetic plateaus and conversion to an ash-free basis. Because the AP route is carried out in 2 M $H_2SO_4$ and no acid-only control was run, demineralisation and sulfur retention belong to that route as practised rather than to the persulfate ion. Surface oxygen content and surface charge, the two quantities by which oxidised chars are normally reported, did not register the largest change that the treatments produced here. An ash determination, phase-resolved diffraction and an ash-scaled elemental analysis did.

## ACKNOWLEDGMENTS

The authors thank Institut Teknologi Sumatera for access to the laboratory and characterisation facilities used in this work. This research received no specific grant from any funding agency in the public, commercial or not-for-profit sectors.

## CONFLICT OF INTEREST

The authors declare that they have no known competing financial interests or personal relationships that could have appeared to influence the work reported in this paper.

## REFERENCES

[1] Dogu O, Pelucchi M, Van de Vijver R, Van Steenberge PHM, D'hooge DR, Cuoci A, Mehl M, Frassoldati A, Faravelli T, Van Geem KM. The chemistry of chemical recycling of solid plastic waste via pyrolysis and gasification: state-of-the-art, challenges, and future directions. *Progress in Energy and Combustion Science*. 2021;84:100901. doi:10.1016/j.pecs.2020.100901.

[2] Laghezza M, Fiore S, Berruti F. A review on the pyrolytic conversion of plastic waste into fuels and chemicals. *Journal of Analytical and Applied Pyrolysis*. 2024;179:106479. doi:10.1016/j.jaap.2024.106479.

[3] Martín-Lara MA, Piñar A, Ligero A, Blázquez G, Calero M. Characterization and use of char produced from pyrolysis of post-consumer mixed plastic waste. *Water*. 2021;13:1188. doi:10.3390/w13091188.

[4] Solís RR, Martín-Lara MÁ, Ligero A, Balbís J, Blázquez G, Calero M. Revalorizing a pyrolytic char residue from post-consumer plastics into activated carbon for the adsorption of lead in water. *Applied Sciences*. 2022;12:8032. doi:10.3390/app12168032.

[5] Barracco F, Parisi E, Pipitone G, Simone E, Bensaid S, Fino D. Valorization of pyrolytic plastic-derived char for adsorption of wastewater contaminants: a kinetic and thermodynamic investigation. *International Journal of Environmental Science and Technology*. 2024;21:6513-6530. doi:10.1007/s13762-024-05467-1.

[6] Abbas-Abadi MS, Kusenberg M, Zayoud A, Roosen M, Vermeire F, Madanikashani S, Kuzmanović M, Parvizi B, Kresovic U, De Meester S, Van Geem KM. Thermal pyrolysis of waste versus virgin polyolefin feedstocks: The role of pressure, temperature and waste composition. *Waste Management*. 2023;165:108-118. doi:10.1016/j.wasman.2023.04.029.

[7] Ye L, Li T, Hong L. Understanding enhanced char formation in the thermal decomposition of PVC resin: Role of intermolecular chlorine loss. *Materials Today Communications*. 2021;26:102186. doi:10.1016/j.mtcomm.2021.102186.

[8] Jabłońska B, Poznańska G, Jabłoński P, Gęga J. Activated Carbon from Pyrolysis of Plastic Waste as an Adsorbent for the Removal of Pb(II), Cd(II) and Co(II) from Aqueous Solutions. *Materials*. 2026;19:3522. doi:10.3390/ma19163522.

[9] Yousef S, Eimontas J, Subadra SP, Striūgas N. Functionalization of char derived from pyrolysis of metallised food packaging plastics waste and its application as a filler in fiberglass/epoxy composites. *Process Safety and Environmental Protection*. 2021;147:723-733. doi:10.1016/j.psep.2021.01.009.

[10] Simanjuntak FFNS, Nasution AH, Ngoc HM, Ichwani R, Kaus NHM, Taher T, Handoko CT, Khair H, Herlina N, Nurfahasdi M, Huda A. The investigation of pyrolytic char quality from mixed non-recycling plastic waste and its thermal treatment through secondary thermal pyrolytic process to activate as an adsorbent for tetracycline pollutant removal. *Next Materials*. 2026;10:101573. doi:10.1016/j.nxmate.2025.101573.

[11] Lillo-Ródenas MA, Cazorla-Amorós D, Linares-Solano A. Understanding chemical reactions between carbons and NaOH and KOH: An insight into the chemical activation mechanism. *Carbon*. 2003;41(2):267-275. doi:10.1016/S0008-6223(02)00279-8.

[12] Raymundo-Piñero E, Azaïs P, Cacciaguerra T, Cazorla-Amorós D, Linares-Solano A, Béguin F. KOH and NaOH activation mechanisms of multiwalled carbon nanotubes with different structural organisation. *Carbon*. 2005;43(4):786-795. doi:10.1016/j.carbon.2004.11.005.

[13] Dodevski V, Marinović-Cincović M, Janković B. Tailoring textural properties of activated carbon produced from Plane tree (Platanus) seeds using alkali (NaOH) activation with improved post-activation treatment procedure for environmental and energy applications. *Carbon Resources Conversion*. 2026;9:100377. doi:10.1016/j.crcon.2025.100377.

[14] Kurniawan I, Nasution AH, Simanjuntak FFNS, Khair H, Ichwani R, Taher T, Handoko CT, Alifia KA, Gea S, Kaus NHM, Huda A. Transforming pyrolytic char from non-recycled domestic plastic waste into high-performance mesoporous char for competitive dyes adsorption system. *Journal of Analytical and Applied Pyrolysis*. 2026;196:107763. doi:10.1016/j.jaap.2026.107763.

[15] Pereira L, Castillo V, Calero M, Blázquez G, Solís RR, Martín-Lara MÁ. Conversion of char from pyrolysis of plastic wastes into alternative activated carbons for heavy metal removal. *Environmental Research*. 2024;250:118558. doi:10.1016/j.envres.2024.118558.

[16] Mukherjee S, Pal S, Ghosh S, Bhattacharya S, Mondal S, Das P. Synthesis of activated carbon using pyrolytic degradation of multi plastic waste and its removal efficiency of dye. *Waste Management Bulletin*. 2025;3:100214. doi:10.1016/j.wmb.2025.100214.

[17] Moon EJ, Park B. KOH-Activated Carbon from Waste Plastic Pyrolysis Residue: Surface Structure Optimization and Adsorption Properties. *Journal of Korea Society of Waste Management*. 2025;42:285-297. doi:10.9786/kswm.2025.42.6.285.

[18] Moreno-Castilla C, Ferro-Garcia MA, Joly JP, Bautista-Toledo I, Carrasco-Marin F, Rivera-Utrilla J. Activated carbon surface modifications by nitric acid, hydrogen peroxide, and ammonium peroxydisulfate treatments. *Langmuir*. 1995;11:4386-4392. doi:10.1021/la00011a035.

[19] Moreno-Castilla C, Lopez-Ramon MV, Carrasco-Marin F. Changes in surface chemistry of activated carbons by wet oxidation. *Carbon*. 2000;38:1995-2001. doi:10.1016/S0008-6223(00)00048-8.

[20] Gómez-Serrano V, Acedo-Ramos M, López-Peinado AJ, Valenzuela-Calahorro C. Oxidation of activated carbon by hydrogen peroxide. Study of surface functional groups by FT-i.r. *Fuel*. 1994;73(3):387-395. doi:10.1016/0016-2361(94)90092-2.

[21] Wang S, Zhu ZH. Effects of acidic treatment of activated carbons on dye adsorption. *Dyes and Pigments*. 2007;75(2):306-314. doi:10.1016/j.dyepig.2006.06.005.

[22] Yang G, Chen H, Qin H, Feng Y. Amination of activated carbon for enhancing phenol adsorption: Effect of nitrogen-containing functional groups. *Applied Surface Science*. 2014;293:299-305. doi:10.1016/j.apsusc.2013.12.155.

[23] Lv S, Li C, Mi J, Meng H. A functional activated carbon for efficient adsorption of phenol derived from pyrolysis of rice husk, KOH-activation and EDTA-4Na-modification. *Applied Surface Science*. 2020;510:145425. doi:10.1016/j.apsusc.2020.145425.

[24] Li S, Huang L, Zhang H, Huang Z, Jia Q, Zhang S. Adsorption mechanism of methylene blue on oxygen-containing functional groups modified graphitic carbon spheres: Experiment and DFT study. *Applied Surface Science*. 2021;540:148386. doi:10.1016/j.apsusc.2020.148386.

[25] Zahakifar F, Dashtinejad M, Sepehrian H, Samadfam M, Fasihi J, Yadollahi A. Intensification of Cr(VI) adsorption using activated carbon adsorbent modified with ammonium persulfate. *Scientific Reports*. 2024;14(1). doi:10.1038/s41598-024-68105-3.

[26] Murat D, Teğin İ, Saka C. Surface modification of biochars for efficient Cu. *Biomass and Bioenergy*. 2026;211:109208. doi:10.1016/j.biombioe.2026.109208.

[27] Hu Z, Tang X, Gao S, Li Y, Wang J, Chen Y, Wang Y. Ammonium Persulfate Modified Activated Carbon for Adsorption of Acrylate VOCs. *Journal of Wuhan University of Technology-Mater. Sci. Ed.*. 2025;40:1176-1185. doi:10.1007/s11595-025-3155-z.

[28] Zhang Y, Qu Y, Wang J, Wang D. Adsorption of bromate in water using hydrogen peroxide-modified activated carbon. *CyTA - Journal of Food*. 2025;23:2499731. doi:10.1080/19476337.2025.2499731.

[29] Derylo-Marczewska A, Swiatkowski A, Trykowski G, Biniak S. The Effect of Oxidative Modification of Activated Carbon on Adsorption of Aromatic Compounds from Aqueous Solutions. *Molecules*. 2025;30:3810. doi:10.3390/molecules30183810.

[30] Ben Ali M, Benzaouak A, Tangarfa M, Abrouki Y, Belekbir S, hazzat ME, El Hamidi A, Abdelouahed L. Multi-response optimization of the adsorption properties of activated carbon produced from H2SO4 activated sludge: Effects of washing with HCl. *Case Studies in Chemical and Environmental Engineering*. 2025;11:101219. doi:10.1016/j.cscee.2025.101219.

[31] Zhou T, Lu Z, Bao Z, Li Y, Chen J, Yao S. Universal correlation between char oxidation reactivity and carbon structure after demineralization: From model compounds to biomasses. *Biomass and Bioenergy*. 2026;210:109088. doi:10.1016/j.biombioe.2026.109088.

[32] Premlall K, Koech L. Influence of coal rank, ash, mineral content, and maceral composition on CO2 adsorption in South African coals. *Cleaner Chemical Engineering*. 2025;11:100160. doi:10.1016/j.clce.2025.100160.

[33] Normah N, Palapa NR, Taher T, Mohadi R, Utami HP, Lesbani A.

 

The Ability of Composite Ni/Al-carbon based Material Toward Readsorption of Iron(II) in Aqueous Solution. *Science and Technology Indonesia*. 2021;6(3):156-165. doi:10.26554/sti.2021.6.3.156-165.

[34] Laila S, Muhtar SA, Irhamni I, Rianjanu A, Saraswati AR, Taher T. Valorization of Indonesian Cassava (Manihot esculenta) Stem Waste into Activated Carbon for Efficient Antibiotic Removal from Aqueous Media. *Green and Sustainable Environments*. 2026;1(1). doi:10.62755/gsenv.2026.01.

[35] Palapa NR, Taher T, Wijaya A, Lesbani A. Modification of Cu/Cr Layered Double Hydroxide by Keggin Type Polyoxometalate as Adsorbent of Malachite Green from Aqueous Solution. *Science and Technology Indonesia*. 2021;6(3):209-217. doi:10.26554/sti.2021.6.3.209-217.

[36] Arif MF, Muhtar SA, Siburian C, Marpaung KDP, Yulianto N, Abdi FF, Taher T, Wasisto HS, Rianjanu A. Zeolite-PAN/PVDF composite nanofiber membranes for highly efficient and selective removal of cationic dyes from wastewater. *Case Studies in Chemical and Environmental Engineering*. 2024;10:100806. doi:10.1016/j.cscee.2024.100806.

[37] Taher T, Yu Z, Melati EKA, Munandar A, Aflaha R, Triyana K, Wibowo YG, Khairurrijal K, Lesbani A, Rianjanu A. Enabling dual-functionality material for effective anionic and cationic dye removal by using Nb2O5/MgAl-LDH nanocomposites. *Journal of Hazardous Materials Letters*. 2024;5:100103. doi:10.1016/j.hazl.2024.100103.

[38] Zerin NH, Rasul MG, Jahirul MI, Sayem ASM, Quadir Z, Haque R. XRD Characterization of Activated Carbons Synthesized from Tyre Pyrolysis Char via KOH Activation. *Technologies*. 2025;13:565. doi:10.3390/technologies13120565.

[39] Kenganal SS, Tiwari A, Sahoo A, Chinthala M. Co-pyrolysis of tea waste and metallised plastic waste: Product characterization, kinetic analysis, and activated carbon applications. *Journal of Environmental Management*. 2026;404:129468. doi:10.1016/j.jenvman.2026.129468.

[40] Chand M, Kumawat A, Srivastava S. Zeta potential-mediated comparative adsorption study of cationic (Methylene blue) and anionic (Congo red) dye onto spent tea (Camellia sinensis) leaves powder. *Surfaces and Interfaces*. 2026;80:108271. doi:10.1016/j.surfin.2025.108271.

[41] Taher T, Oktaviani T, Putri SE, Pratiwi AS, Muhtar SA, Huda A, Kurnia I, Waluyo J, Rianjanu A. Beyond surface area and surface charge: Oxidant-dependent methylene-blue uptake on a TiO. *Applied Surface Science*. 2026:168313. doi:10.1016/j.apsusc.2026.168313.

[42] Bergmann J, Friedel P, Kleeberg R. BGMN — a new fundamental parameters based Rietveld program for laboratory X-ray sources, its use in quantitative analysis and structure investigations. *CPD Newsletter*. 1998;20:5-8.

[43] De La Torre AG, Bruque S, Aranda MAG. Rietveld quantitative amorphous content analysis. *Journal of Applied Crystallography*. 2001;34(2):196-202. doi:10.1107/s0021889801002485.

[44] Ho YS, McKay G. Pseudo-second order model for sorption processes. *Process Biochemistry*. 1999;34(5):451-465. doi:10.1016/s0032-9592(98)00112-5.

[45] Simonin JP. On the comparison of pseudo-first order and pseudo-second order rate laws in the modeling of adsorption kinetics. *Chemical Engineering Journal*. 2016;300:254-263. doi:10.1016/j.cej.2016.04.079.

[46] Tran HN, You SJ, Hosseini-Bandegharaei A, Chao HP. Mistakes and inconsistencies regarding adsorption of contaminants from aqueous solutions: A critical review. *Water Research*. 2017;120:88-116. doi:10.1016/j.watres.2017.04.014.

[47] Weber WJ, Morris JC. Kinetics of adsorption on carbon from solution. *Journal of the Sanitary Engineering Division*. 1963;89(2):31-59. doi:10.1061/JSEDAI.0000430.

[48] Langmuir I. THE ADSORPTION OF GASES ON PLANE SURFACES OF GLASS, MICA AND PLATINUM. *Journal of the American Chemical Society*. 1918;40(9):1361-1403. doi:10.1021/ja02242a004.

[49] Foo KY, Hameed BH. Insights into the modeling of adsorption isotherm systems. *Chemical Engineering Journal*. 2010;156(1):2-10. doi:10.1016/j.cej.2009.09.013.

[50] Liyanaarachchi H, Thambiliyagodage C, Lokuge H, Vigneswaran S. Kinetics and Thermodynamics Study of Methylene Blue Adsorption to Sucrose- and Urea-Derived Nitrogen-Enriched, Hierarchically Porous Carbon Activated by KOH and H. *ACS Omega*. 2023;8(18):16158-16173. doi:10.1021/acsomega.3c00339.

[51] El-Bery HM, Saleh M, El-Gendy RA, Saleh MR, Thabet SM. High adsorption capacity of phenol and methylene blue using activated carbon derived from lignocellulosic agriculture wastes. *Scientific Reports*. 2022;12(1). doi:10.1038/s41598-022-09475-4.

[52] Bhattacharjee S. DLS and zeta potential – What they are and what they are not?. *Journal of Controlled Release*. 2016;235:337-351. doi:10.1016/j.jconrel.2016.06.017.

[53] Lowry GV, Hill RJ, Harper S, Rawle AF, Hendren CO, Klaessig F, Nobbmann U, Sayre P, Rumble J. Guidance to improve the scientific value of zeta-potential measurements in nanoEHS. *Environmental Science: Nano*. 2016;3(5):953-965. doi:10.1039/c6en00136j.

[54] Biscoe J, Warren BE. An X-ray study of carbon black. *Journal of Applied Physics*. 1942;13(6):364-371. doi:10.1063/1.1714879.

[55] Li ZQ, Lu CJ, Xia ZP, Zhou Y, Luo Z. X-ray diffraction patterns of graphite and turbostratic carbon. *Carbon*. 2007;45(8):1686-1695. doi:10.1016/j.carbon.2007.03.038.

[56] Musić S, Filipović-Vinceković N, Sekovanić L. Precipitation of amorphous SiO2 particles and their properties. *Brazilian Journal of Chemical Engineering*. 2011;28(1):89-94. doi:10.1590/S0104-66322011000100011.

[57] Okamura M, Takagaki A, Toda M, Kondo JN, Domen K, Tatsumi T, Hara M, Hayashi S. Acid-catalyzed reactions on flexible polycyclic aromatic carbon in amorphous carbon. *Chemistry of Materials*. 2006;18(13):3039-3045. doi:10.1021/cm0605623.

[58] Fantauzzi M, Elsener B, Atzei D, Rigoldi A, Rossi A. Exploiting XPS for the identification of sulfides and polysulfides. *RSC Advances*. 2015;5(93):75953-75963. doi:10.1039/C5RA14915K.

[59] Gao JJ, Qin YB, Zhou T, Cao DD, Xu P, Hochstetter D, Wang YF. Adsorption of methylene blue onto activated carbon produced from tea (Camellia sinensis L.) seed shells: kinetics, equilibrium, and thermodynamics studies. *Journal of Zhejiang University Science B*. 2013;14:650-658. doi:10.1631/jzus.B12a0225.

[60] Lawtae P, Tangsathitkulchai C. The use of high surface area mesoporous-activated carbon from longan seed biomass for increasing capacity and kinetics of methylene blue adsorption from aqueous solution. *Molecules*. 2021;26:6521. doi:10.3390/molecules26216521.

[61] He Y, Ni L, Gao Q, Ren H, Su M, Hou Y, Liu Z. Activated carbon with ultrahigh specific surface derived from bamboo shoot shell through K2FeO4 oxidative pyrolysis for adsorption of methylene blue. *Molecules*. 2023;28:3410. doi:10.3390/molecules28083410.

[62] Ji B, Wang J, Song H, Chen W. Removal of methylene blue from aqueous solutions using biochar derived from a fallen leaf by slow pyrolysis: behavior and mechanism. *Journal of Environmental Chemical Engineering*. 2019;7:103036. doi:10.1016/j.jece.2019.103036.

[63] Arias Arias F, Guevara M, Tene T, Angamarca P, Molina R, Valarezo A, Salguero O, Vacacela Gomez C, Arias M, Caputi LS. The adsorption of methylene blue on eco-friendly reduced graphene oxide. *Nanomaterials*. 2020;10:681. doi:10.3390/nano10040681.

[64] Gutierrez-Martinez J, Martinez-Vargas DR, Vences-Alvarez E, Arjona-Jaime P, López-Cázares MI, Rios-Saldaña LE, Isaacs-Páez ED, Quijano-Meza M, Rocha-Medina C, Rangel-Mendez R. Point of zero charge, isoelectric point, and potential of zero charge on activated carbons: A comprehensive interpretation about their interrelation. *Current Opinion in Solid State and Materials Science*. 2026;40:101247. doi:10.1016/j.cossms.2025.101247.

[65] Kosmulski M. The pH dependent surface charging and points of zero charge. XI. Update. *Advances in Colloid and Interface Science*. 2026;353:103878. doi:10.1016/j.cis.2026.103878.

 